nature communications

Article

https://doi.org/10.1038/s41467-024-50771-6

High-affinity agonism at the $P2X_7$ receptor is mediated by three residues outside the orthosteric pocket

Received: 7 January 2024

Accepted: 19 July 2024

Published online: 06 August 2024

Check for updates

Adam C. Oken[1], Nicolas E. Lisi[1], Ipsita Krishnamurthy[1], Alanna E. McCarthy[2], Michael H. Godsey[1], Arthur Glasfeld[1] & Steven E. Mansoor[1,2]

P2X receptors are trimeric ATP-gated ion channels that activate diverse signaling cascades. Due to its role in apoptotic pathways, selective activation of $P2X_7$ is a potential experimental tool and therapeutic approach in cancer biology. However, mechanisms of high-affinity $P2X_7$ activation have not been defined. We report high-resolution cryo-EM structures of wild-type rat $P2X_7$ bound to the high-affinity agonist BzATP as well as significantly improved apo receptor structures in the presence and absence of sodium. Apo structures define molecular details of pore architecture and reveal how a partially hydrated Na^+ ion interacts with the conductance pathway in the closed state. Structural, electrophysiological, and direct binding data of BzATP reveal that three residues just outside the orthosteric ATP-binding site are responsible for its high-affinity agonism. This work provides insights into high-affinity agonism for any P2X receptor and lays the groundwork for development of subtype-specific agonists applicable to cancer therapeutics.

ATP, the primary source of energy within cells, has a well-established and central role as an intracellular metabolite[1]. However, ATP is also important in the extracellular environment as a signaling molecule[2–5]. Extracellular ATP (eATP) is recognized by two purinergic receptor families: ligand-gated P2X receptor (P2XR) ion channels and G-protein coupled P2Y receptors[5–9]. The seven P2XR subtypes, denoted $P2X_1$-$P2X_7$, are non-selective cation channels that are expressed throughout the body and assemble as functional homotrimeric and heterotrimeric receptors[5,8,10–12]. Each P2XR subtype is activated by distinct concentrations of eATP and then desensitizes with unique kinetics determined by the underlying receptor subunit composition[8,13–19]. The functional diversity of P2XRs directly contributes to their roles in numerous physiological and pathophysiological processes from synaptic transmission to asthma and atherosclerosis to cancer[8,12,20–26]. As such, P2XRs are promising clinical targets for diseases of the immune, cardiovascular, and central nervous systems[20,25,27–29].

The orthosteric ATP-binding site is a conserved feature across all P2XRs, yet there is significant pharmacological diversity for agonists within this receptor family[8,13–15,19,30,31]. Subtype-specific P2XR activation is governed by differences in tissue-dependent expression and by a variance in half maximal response (apparent affinity, EC_{50}) to eATP between subtypes[8,13,15,19,32]. For example, while $P2X_1$ and $P2X_3$ are activated by nanomolar concentrations of eATP, $P2X_2$, $P2X_4$, $P2X_5$, and $P2X_6$ are activated by low micromolar levels of eATP, and $P2X_7$ is only activated by mid-micromolar to low-millimolar levels of eATP[13]. Further evidence for pharmacological diversity lies in how specific P2XR subtypes interact with well-established synthetic nucleotide-analog agonists such as 2–MeS-ATP, α,β-MeATP, β,γ-MeATP, and BzATP (Supplementary Fig. 1)[8,13,15,19,33]. For example, BzATP is reported to be a high-affinity agonist across all P2XRs, while α,β-MeATP is selective towards $P2X_1$ and $P2X_3$[13,15,19]. The mechanisms underlying agonist selectivity and high-affinity agonism for P2XRs are not defined.

Once termed the P2Z receptor due to its markedly distinct properties relative to other P2X family members, $P2X_7$ is the most structurally and functionally divergent P2XR[8,30,34]. In addition to requiring the highest concentrations of eATP for activation, $P2X_7$ is the only subtype that does not desensitize in the prolonged presence of agonist[19,35]. These features facilitate numerous $P2X_7$-mediated cellular

[1]Department of Chemical Physiology & Biochemistry, Oregon Health & Science University, Portland, OR 97239, USA. [2]Division of Cardiovascular Medicine, Knight Cardiovascular Institute, Oregon Health & Science University, Portland, OR 97239, USA. e-mail: mansoors@ohsu.edu

responses such as signaling the formation of the NLRP3 inflammasome and triggering apoptosis[36,37]. The $P2X_7$-mediated activation of these processes has therapeutic potential within the field of cancer biology[24,26]. For example, in melanoma/colon cancer, acute myeloid leukemia, and breast cancer, $P2X_7$ activation promotes tumor cell death, leads to apoptosis of cancerous cells, or decreases cancerous cell migration, respectively[38–40]. As such, $P2X_7$-selective high-affinity agonists are important experimental tools and a potential therapeutic approach that warrant investigation to further advance the field of cancer biology.

The orthosteric ATP-binding site of $P2X_7$ has been described by several groups, each using a different $P2X_7$ ortholog with varying amounts of protein engineering required to facilitate analysis[35,41,42]. A crystal structure of both ATP and the allosteric antagonist A804598 simultaneously bound to panda $P2X_7$ ($pdP2X_7$) initially defined the orthosteric ATP-binding pocket of $pdP2X_7$, albeit in a functionally complicated state with a significantly truncated construct used for crystallization[41]. As a result, the construct does not possess wild-type ion channel function, contains noticeably short transmembrane helices, and prevents visualization of the receptor's entire cytoplasmic domain[41]. Similarly, a crystal structure of chicken $P2X_7$ bound to low-affinity orthosteric antagonist TNP-ATP was solved using a truncated construct but provided insights into orthosteric antagonism (Supplementary Fig. 1)[42]. Using the same aforementioned $pdP2X_7$ construct, recent single-particle cryogenic electron microscopy (cryo-EM) structures of PPNDS and PPADS bound to $pdP2X_7$ provide additional insights into orthosteric antagonism (Supplementary Fig. 1)[43]. In contrast to truncated constructs, the cryo-EM structure of full-length wild-type rat $P2X_7$ ($rP2X_7$) bound to ATP resulted in a true open state model of the entire receptor, clearly illustrating the receptor gating cycle, the orthosteric ligand-binding site, as well as visualizing the cytoplasmic domains referred to as the C-cys anchor and the cytoplasmic ballast[35]. In each of these previous studies, agonist-bound structures have been limited to ATP only, and so we have yet to fully understand how high-affinity agonists modulate $P2X_7$ activity at a molecular level.

Seeking enhanced molecular details of full-length wild-type $P2X_7$ receptor-ligand interactions, we use cryo-EM to further reveal the molecular pharmacology of the apo receptor and define high-affinity agonism for $rP2X_7$. Our updated, significantly higher resolution, apo closed state structures of $rP2X_7$, both at 2.5 Å, provide important insights into unoccupied ligand-binding pockets, detailed architecture of the closed pore, and non-proteinaceous features such as bound ions and water molecules. A structure of the high-affinity P2XR agonist BzATP bound to $rP2X_7$ at 2.8 Å reveals key interactions and structural movements that explain the increased affinity and interesting pharmacologic properties of this ligand. These data provide vital molecular details that will empower structure-based drug design of innovative $P2X_7$-modulating ligands.

Results

Architecture of the conductance pathway in the apo closed state of $P2X_7$

To elucidate the molecular mechanisms of small-molecule ligand modulation of $P2X_7$ activity, cryo-EM was used to obtain structural information on the full-length wild-type $rP2X_7$ receptor in apo and high-affinity agonist-bound states (Supplementary Fig. 2, 3, Supplementary Table 1). As expected, the overall architecture common to P2XRs is maintained in $rP2X_7$; each protomer of the receptor resembles a breaching dolphin with structural domains named accordingly (Fig. 1A)[44]. Improving the resolution of the previously published apo

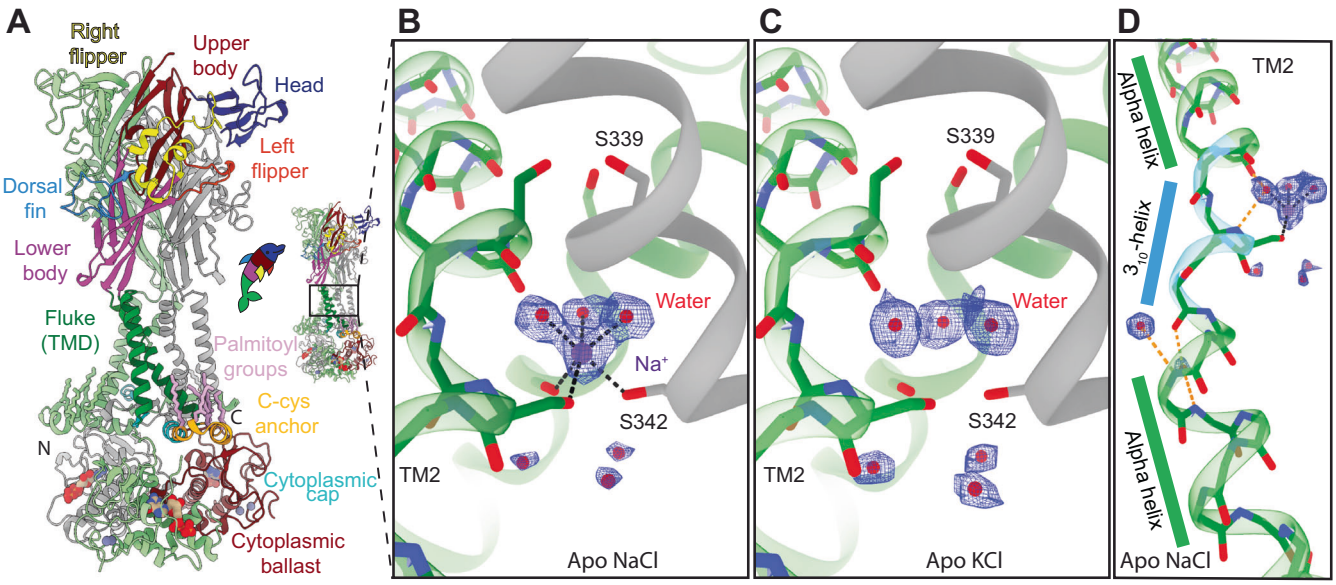

Fig. 1 | Global architecture and Na^+ ion coordination in the apo closed state pore of $rP2X_7$. A Ribbon representation of the updated apo closed state structure of $rP2X_7$ at 2.5 Å, with one protomer colored by domain name, the second colored in pale green, and the third colored in gray. **B** View of the Na^+ ion (purple sphere) found directly above the pore's constriction site (created by TM2 from each protomer) in the apo closed state with its electron density map shown in blue mesh. The Na^+ ion is partially hydrated, coordinated in octahedral geometry by three symmetry-related water molecules (red spheres) and the sidechain hydroxyl of S342 from each protomer (~2.3 Å for all interactions). Directly below the gate and within the pore, three additional symmetry-related water molecules are poised to re-hydrate the ion once the channel opens (3 Å hydrogen bond distance to the sidechain hydroxyl of S342). **C** The same view as in panel (**B**) of apo $rP2X_7$ purified in the absence of sodium, highlighting the lack of density for an ion above the gate. This result confirms the identity of the density shown in panel (**B**) as a partially hydrated Na^+ ion. **D** Zoomed out view of panel (**B**) highlighting the topology of the TM2 helix, stabilized by interactions with three different sets of symmetry-related ordered water molecules, one set within the pore and above the gate and the other two sets below the gate and within the transmembrane domain. TM2 starts as a standard alpha helix (green ribbon), then transitions to a short 3_{10}-helix (cyan ribbon, residues 340–344) just above the constriction gate and shortly after, transitions back to a standard alpha helix (green ribbon) just below the constriction gate. Transitions to and from the 3_{10}-helix are mediated by ordered water molecules within the transmembrane domain that induce kinks in the helical backbone of TM2. Interactions with the protein are in gold dashed lines and interactions for Na^+ coordination are in black dashed lines. All sidechains in TM2 are hidden except for the sidechains of S339 and S342.

https://doi.org/10.1038/s41467-024-50771-6

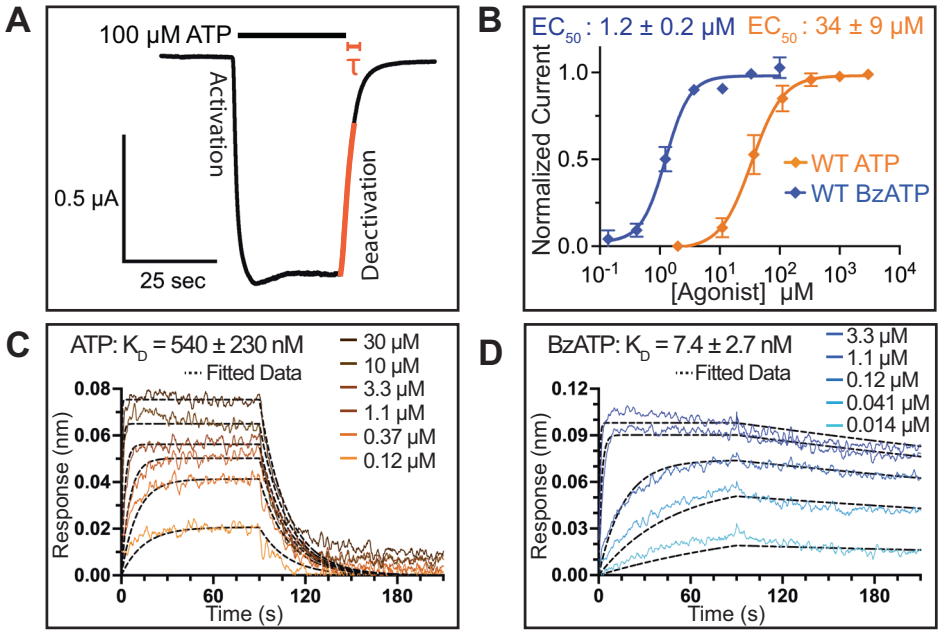

Fig. 2 | Activation and binding kinetics of ATP and BzATP to rP2X$_7$. A TEVC recording of rP2X$_7$ in response to 100 μM ATP, highlighting fast activation after repeated exposure to ATP, no significant desensitization, and brisk deactivation. The reported deactivation lifetime (τ), shown in reddish-orange, is the time it takes for current to return to 63% of baseline after removal of ATP. **B** Dose response curves from TEVC experiments measured the activation of full-length wild-type rP2X$_7$ by ATP (orange) and BzATP (blue), resulting in EC_{50} values of 34 ± 9 μM and 1.2 ± 0.2 μM, respectively. Data points and error bars represent the mean and standard deviation of normalized current across triplicate experiments, respectively. **C**, **D** Representative BLI sensorgrams for a dilution series of ATP (**C**, shades of orange) and BzATP (**D**, shades of blue) binding to biotinylated rP2X$_7$ immobilized on streptavidin (SA) biosensors. Kinetic data were globally fit using a Langmuir 1:1 model to determine the equilibrium dissociation constant (K_D) of ATP to rP2X$_7$ as K_D = 540 ± 230 nM (**C**) and the equilibrium dissociation constant of BzATP to rP2X$_7$ as K_D = 7.4 ± 2.7 nM (**D**), representing the mean and standard deviation across triplicate experiments, respectively. For kinetic analysis, a 90 s association time and a 200 s dissociation time were used for both analytes. However, to optimize visualization, only 120 s of the dissociation time is shown in the figure.

closed state structure of rP2X$_7$ from 2.9 Å to 2.5 Å uncovered details that significantly improve the apo closed state model for this P2XR subtype (Supplementary Fig. 2, 3, Supplementary Table 1)[35]. For example, numerous water molecules absent in the original published model are easily placed into density throughout the receptor, especially in the unoccupied allosteric and orthosteric ligand-binding sites. In addition to improvements that yield a better starting point for structure-based drug design, the higher resolution apo closed state data for the rP2X$_7$ receptor also provides insights into the conductance pathway and a much clearer snapshot of the unique architecture of the closed pore[45,46].

In our updated high-resolution structure for the apo closed state conformation of rP2X$_7$ in the presence of sodium, an ion can be observed in the center of the pore, poised directly above the closed constriction site (gate) formed by the second transmembrane helix (TM2) from each protomer (Fig. 1B). The ion is coordinated in near-perfect octahedral geometry by three symmetry-related ordered water molecules and the sidechain hydroxyl of S342 from each protomer, suggesting the presence of a partially hydrated Na^+ ion (Fig. 1B)[47]. Ion coordination was used to confirm the identity of Na^+ with the CheckMyMetal validation server[48]. To further confirm its identity as a Na^+ ion, a second cryo-EM structure of rP2X$_7$ in the apo closed state, purified in the absence of sodium, was obtained at 2.5 Å (Fig. 1C, Supplementary Fig. 2, 3, Supplementary Table 1). The map refined from this data shows no significant density at this position indicating the absence of the previously observed ion (Fig. 1C). Of note, the ordered water molecules that interact with the Na^+ ion remain in the absence of sodium (Fig. 1B, C). Additionally, in both high-resolution apo closed state rP2X$_7$ structures (in the presence and absence of sodium), symmetry-related water molecules located within the pore and just 3 Å below the gate, interact with the sidechain hydroxyl of S342 from the corresponding protomer (Fig. 1B, C).

In addition to features such as a partially hydrated Na^+ ion, the architecture of the apo closed state pore, formed by TM2 from each protomer, can be updated to explain its unique helical structure. The set of symmetry-related ordered water molecules that are located within the pore and above the receptor gate (discussed above), coordinate the Na^+ ion and interact with the backbone carbonyl of G338 and the backbone nitrogen of S342 (Fig. 1D, Supplementary Fig. 4A). These water/protein interactions interrupt standard alpha helical hydrogen bonding patterns and induce a short 3_{10}-helix in TM2 (residues 340–344) (Fig. 1D, Supplementary Fig. 4A). Shortly after its initiation, the 3_{10}-helix in TM2 transitions back to a standard alpha helix, facilitated by two additional sets of symmetry-related ordered water molecules, both of which are located below the gate and within the transmembrane domain (Fig. 1D, Supplementary Fig. 4B). The first set of these waters partially replaces the hydrogen bonding expected to be present in a standard alpha helix, interacting with the amide nitrogen of A347 as well as a sidechain nitrogen of H34 from the first transmembrane helix (TM1) (Supplementary Fig. 4B). This set of waters does not coordinate to the backbone carbonyls of either Y343 (due to an inappropriate hydrogen bonding distance) or F344 (due to an inappropriate hydrogen bonding angle) (Supplementary Fig. 4B). The second set of these waters interacts with the carbonyl of F344 and the amide nitrogen of T348, replacing the hydrogen bonding expected for a standard alpha helix (Supplementary Fig. 4B). Transitions to and from the 3_{10}-helix, facilitated by the three aforementioned sets of ordered water molecules, one set within the pore and above the gate and the other two sets below the gate and within the transmembrane domain, induce corresponding kinks in the helical backbone of TM2 (Fig. 1D, Supplementary Fig. 4). The short 3_{10}-helix is present in models obtained both in the presence and absence of sodium and likely plays a key role to correctly position S342 from

https://doi.org/10.1038/s41467-024-50771-6

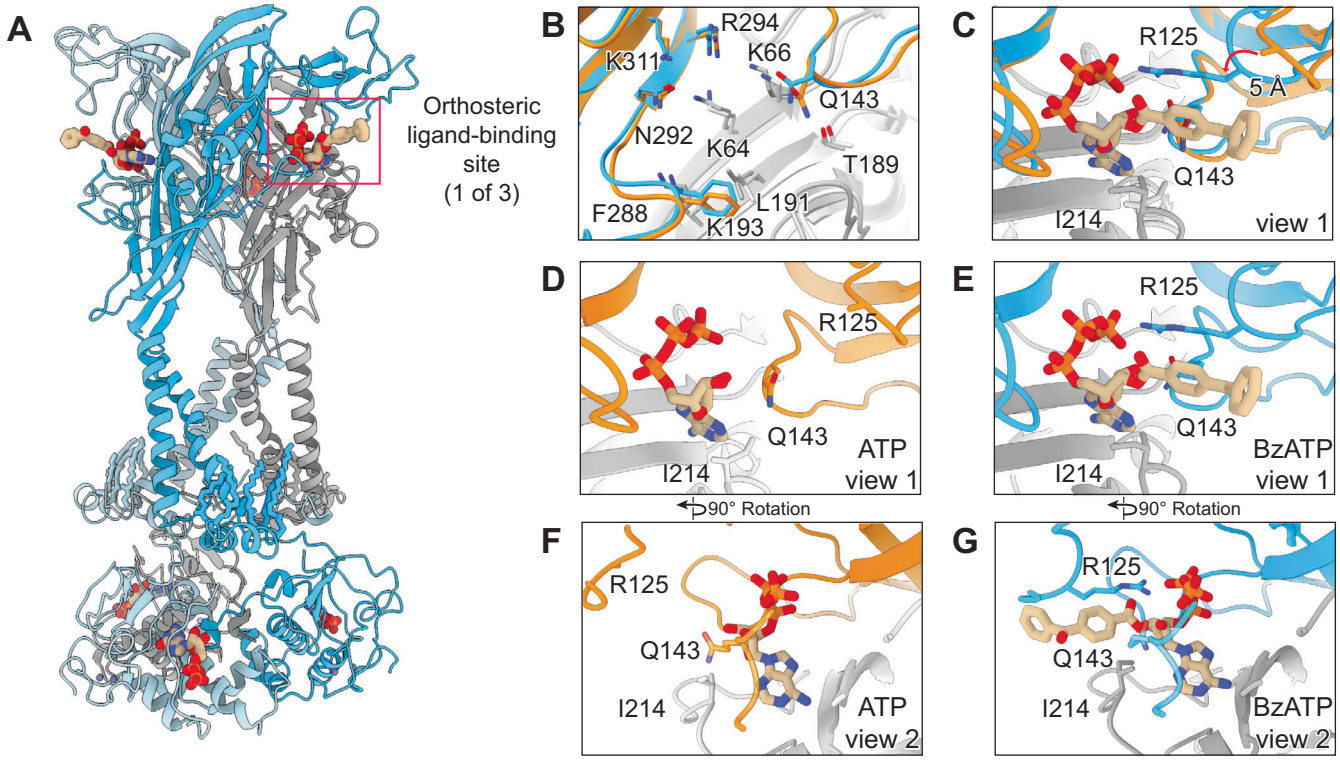

Fig. 3 | Structural comparison of rP2X$_7$ bound to BzATP vs ATP. A Ribbon representation of the BzATP-bound open state structure of rP2X$_7$ solved to 2.8 Å colored by protomer (blue, light-blue, and gray) highlighting the orthosteric ligand-binding site (red box). **B**–**E** Magnified view of the red box from (**A**) at different scales. The ATP-bound rP2X$_7$ structure (PDB code: 6U9W) and the BzATP-bound rP2X$_7$ structure were aligned in ChimeraX[70]. **B** Comparison of positions and rotamers of residues in the orthosteric ligand-binding site (ligands hidden), which are conserved across all P2XRs, that directly interact with ATP for the ATP-bound rP2X$_7$ structure (orange and light gray) and the BzATP-bound rP2X$_7$ structure (blue and gray). In the register of rP2X$_7$, the conserved orthosteric residues that interact with ATP across all P2XRs are K64, K66, T189, K193, N292, R294, K311. **C** Comparison of ATP-bound (orange) and BzATP-bound (blue) structures, focusing on the residues just outside the canonical orthosteric ligand-binding site that make direct interactions with BzATP. With the ATP molecule hidden but the BzATP molecule shown, the panel highlights the 5 Å movement and 90° rotation of a loop in the head domain (residues 123–128) containing residue R125 that occurs when BzATP is bound. In the ATP-bound model, R125 is stubbed at the Cβ carbon. First comparative view (**D**, **E**) and second comparative view (**F**, **G**), rotated 90 degrees from (**C**–**E**), of the rP2X$_7$ orthosteric ligand-binding site with ATP bound (orange and light gray) vs. BzATP bound (blue and gray). **D** View of the orthosteric ligand-binding site of ATP-bound rP2X$_7$ highlighting the rotamer of I214 and the position of R125, which lacks interactions with ATP. **E** View of the orthosteric ligand-binding site of BzATP-bound rP2X$_7$ highlighting the rotamer of I214 and the position of R125, which is now well-defined. **F** View of the orthosteric ligand-binding site of ATP-bound rP2X$_7$ highlighting the rotamer of Q143, facing away from ATP, unable to make direct interactions to ATP. **G** View of the orthosteric ligand-binding site of BzATP-bound rP2X$_7$ highlighting the position and rotamer of Q143, now participating in several hydrogen bonding interactions with BzATP and residue R125.

each protomer to form the gate in the apo closed state conformation (Fig. 1B–D). Altogether, the interplay between TM2 of P2X$_7$, ordered water molecules both above and below the gate, and a partially hydrated Na^+ ion reveal unique properties of the apo closed state pore.

Measurements of activation and binding of ATP and BzATP to P2X$_7$

P2X$_7$ has distinct electrophysiological properties compared to other P2XRs. In the presence of sufficient levels of eATP, P2X$_7$ remains open and does not undergo desensitization (Fig. 2A)[35]. Upon removal of eATP, rP2X$_7$ undergoes brisk deactivation, returning to an apo closed state at a rate which can be quantified by the deactivation lifetime (τ), the time it takes for the current to return to 63% of baseline (Fig. 2A). Using two-electrode voltage clamp (TEVC), the EC_{50} of ATP and BzATP for wild-type rP2X$_7$ are measured to be 34 ± 9 μM and 1.2 ± 0.2 μM, respectively, consistent with previously published values (Fig. 2B)[13,35]. By TEVC, BzATP has ~28-fold higher apparent affinity than ATP.

To date, no direct measurements of ligand binding to P2X$_7$ have been reported. To address this issue, the kinetics and equilibrium binding affinity of ATP and BzATP to rP2X$_7$ were measured by bio-layer interferometry (BLI) (Fig. 2C, D)[49]. The rate constant for association (k_a) of ATP to rP2X$_7$ is 9.4 ± 2.4 x10^4 $M^{-1}s^{-1}$ and its rate constant for dissociation (k_d) is 5.1 ± 2.5 x10^{-2} s^{-1}, resulting in binding to the receptor with an affinity (K_D = 540 ± 230 nM) approximately 190-fold lower than that of human P2X$_3$ (K_D = 2.8 ± 0.1 nM) and 46-fold lower than that of zebra fish P2X$_4$ (K_D = 11.6 ± 1.7 nM) (Fig. 2C)[50,51]. The rate of association for ATP is consistent with previously generated values from electrophysiological models[52]. BzATP is known to be a more potent P2X$_7$ agonist than ATP, and correspondingly we show it associates more rapidly (k_a of 3.7 ± 1.0 x10^5 $M^{-1}s^{-1}$) with the receptor and dissociates more slowly (k_d of 2.6 ± 1.0 x10^{-3} s^{-1}) from the receptor, resulting in a ~70-fold higher binding affinity (K_D = 7.4 ± 2.7 nM) (Fig. 2D)[53].

Structural differences between agonists ATP and BzATP bound to P2X$_7$

We used cryo-EM analysis and electrophysiology assays to explain the high-affinity agonism by BzATP for rP2X$_7$. The cryo-EM structure of BzATP bound to rP2X$_7$ was resolved to 2.8 Å and compared to the previously solved ATP-bound structure at 3.3 Å (Fig. 3, Supplementary Fig. 1, 2, 3, 5, 6, Supplementary Table 1) (PBD code: 6U9W)[35]. As expected, the BzATP-bound structure represents an open state conformation (backbone RMSD of ~1.2 Å relative to the ATP-bound structure). The architecture of the open pore in both agonist-bound structures is quite similar (Supplementary Fig. 5). Within the orthosteric ligand-binding site, the positions and rotamers of each amino acid

https://doi.org/10.1038/s41467-024-50771-6

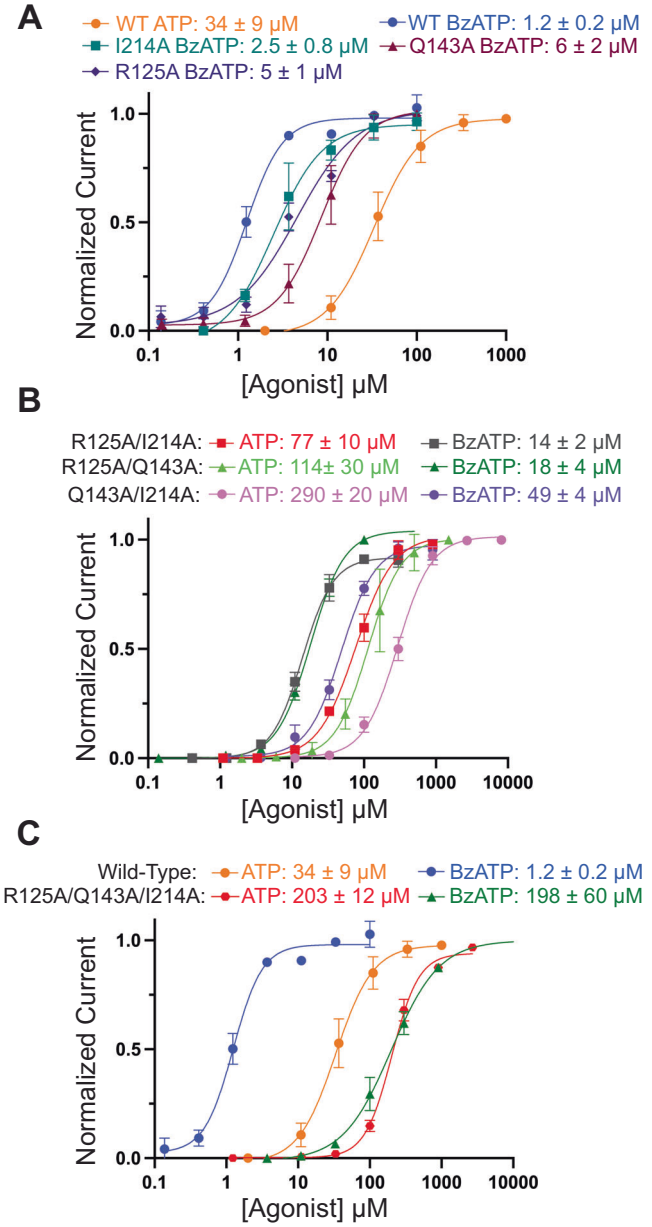

Fig. 4 | Apparent affinities (EC_{50}) of rP2X$_7$ activation by ATP and BzATP. A Dose-response curves (EC_{50}) for wild-type rP2X$_7$ activated by ATP and BzATP as well as the three single mutant receptors (R125A, Q143A, and I214A) activated by BzATP. These traces highlight the impact of specific residues just outside the canonical orthosteric ligand-binding site on the apparent affinity of the receptor for BzATP. No single residue mutation is able to fully abrogate the higher apparent affinity of BzATP relative to ATP. **B** Dose-response curves (EC_{50}) for the three double mutant receptors (R125A/Q143A, R125A/I214A, and Q143A/I214A) activated by ATP and BzATP. While each of the double mutant receptors demonstrated a decreased apparent affinity for ATP relative to wild-type rP2X$_7$ receptor (Table 1), in each case, the corresponding apparent affinity for BzATP always remained significantly higher. **C** Dose-response curves (EC_{50}) for wild-type and triple mutant (R125A/Q143A/I214A) rP2X$_7$ activated by ATP and BzATP highlighting that mutation of all three residues just outside the canonical orthosteric ligand-binding site completely eliminates the high-affinity agonism of BzATP relative to ATP. Note that while the wild-type receptor has a ~28-fold higher apparent affinity for BzATP than ATP, the apparent affinity of the triple mutant receptor (R125A/Q143A/I214A) is essentially identical for ATP and BzATP. The apparent affinity (EC_{50}) values for all wild-type and mutant receptors are included in Table 1. Data points and error bars represent the mean and standard deviation of normalized current across triplicate experiments, respectively.

that directly interacts with ATP are conserved and make the same direct interactions to the adenosine triphosphate core of BzATP (Fig. 3B)[35]. However, three key structural changes in the receptor, found just outside the canonical orthosteric ligand-binding site, are evident when BzATP is bound to rP2X$_7$ when compared to ATP bound to rP2X$_7$.

The largest structural difference is found in a loop (residues 123–128) in the head domain of rP2X$_7$ (Figs. 1A, 3C–G). In the ATP-bound structure, the protein backbone of this loop is well-ordered as it runs parallel to the membrane. However, residue R125 of this loop faces solvent surrounding the orthosteric ligand-binding site, lacking interactions with other residues or with ATP. As a result, the flexible R125 sidechain is without density in the map and is stubbed at the Cβ carbon in the ATP-bound model (Fig. 3C, D, F)[35]. In contrast, with BzATP bound, direct interactions between R125 and BzATP result in a dramatic rearrangement of this loop with the sidechain of R125 rotated nearly 90° relative to the Cα-Cβ bond in the ATP-bound structure (Fig. 3C, E, G)[35]. This rotation displaces the Cβ of R125 by ~5 Å, shifting it towards the orthosteric ligand-binding site and causing the sidechain of R125 to run anti-parallel to the carboxybenzophenone moiety of BzATP, creating several new contacts with the ligand (Fig. 3C, E, G, Supplementary Fig. 1, 6). The location of R125 in the apo closed state is further distinct from its position in either of the two agonist-bound structures (Supplementary Fig. 7). Compared to the apo state structure, the Cβ of R125 moves 5.7 Å closer to the orthosteric pocket in the ATP-bound structure and 7.8 Å closer in the BzATP-bound structure (Supplementary Fig. 7C, D).

The second significant change involves residue Q143 adopting a different conformation between the two ligand-bound structures (Fig. 3C–G). When ATP is bound, the sidechain amide of Q143 points away from the ligand and is too far away to form hydrogen bonding interactions (Fig. 3C, D, F)[35]. When BzATP is bound, however, the steric bulk of the carboxybenzophenone moiety of BzATP forces Q143 to adopt a different conformation such that the sidechain amide points directly at the ribose in BzATP, creating new hydrogen bonding interactions with the ribose as well as the guanidino group of R125 (Fig. 3C, E, G, Supplementary Fig. 6).

The final notable difference between the ATP-bound and BzATP-bound structures involves residue I214, which changes both its position and rotameric conformation relative to the bound ligand (Fig. 3C–G, Supplementary Fig. 6). When ATP is bound in the pocket, I214 is at least 4.3 Å away from the ribose ring of ATP and does not participate in direct hydrophobic interactions with the ligand (Fig. 3C, D, F)[35]. However, when BzATP is bound, I214 adopts a new rotamer and shifts closer to the ligand by 1.1 Å, allowing it to make hydrophobic interactions with the carboxybenzophenone moiety of BzATP (Fig. 3C, E, G, Supplementary Fig. 6).

Based on the two agonist-bound structures, three residues (R125, Q143, and I214) adopt different positions and introduce new protein-ligand interactions with BzATP (Fig. 3C–G). We next wanted to use a combination of site-directed mutagenesis and electrophysiology experiments to explore whether these interactions can explain the increased apparent affinity and direct affinity (measured by EC_{50} and K_D, respectively) and slow rate of dissociation (k_d) observed for BzATP binding to rP2X$_7$ relative to ATP binding.

Agonism of wild-type and mutant P2X$_7$ by BzATP

In silico thermodynamic (ΔΔG) calculations in Rosetta support the importance of residues R125, Q143, and I214 to the coordination of BzATP (Supplementary Table 2)[54]. Systematic alanine mutations were introduced to evaluate the role that each of these residues plays in the pharmacology of BzATP high-affinity agonism using TEVC experiments (Figs. 4, 5, 6, Table 1, Supplementary Fig. 8). Both individual and combinations of mutations were introduced to determine the specific

https://doi.org/10.1038/s41467-024-50771-6

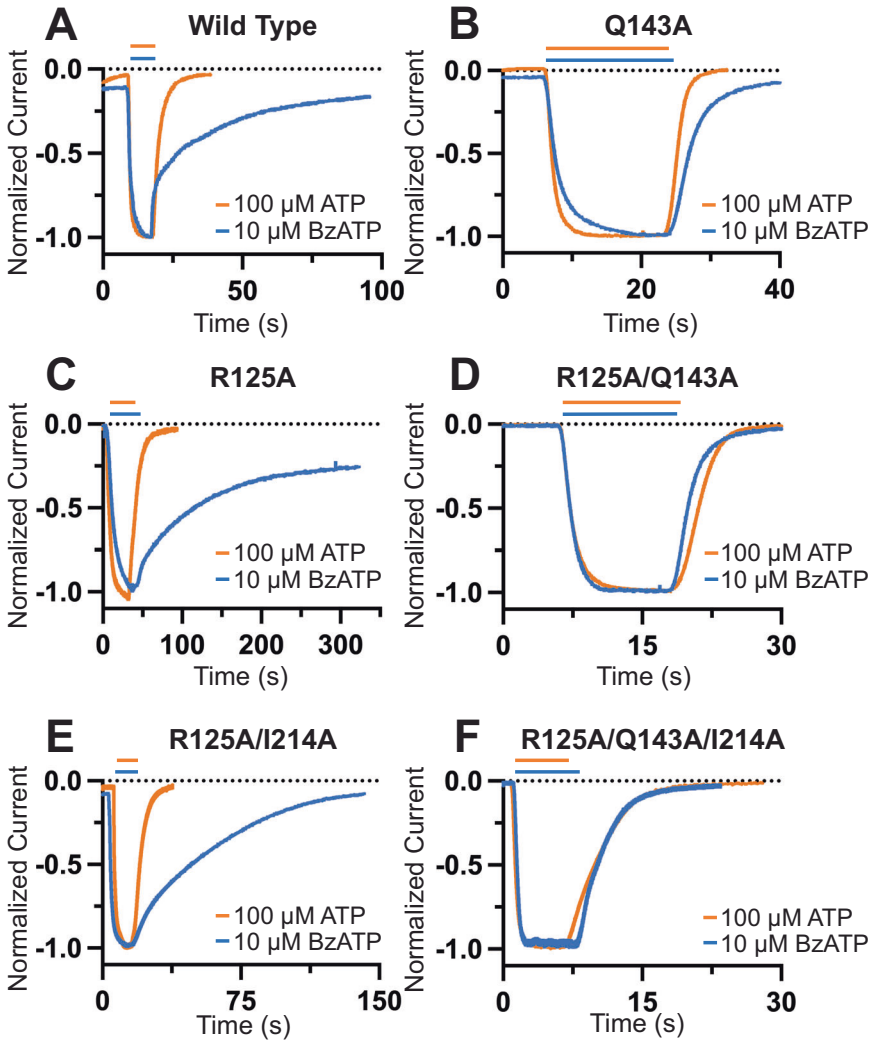

Fig. 5 | Deactivation rates of rP2X$_7$ following activation by ATP and BzATP. **A**–**F** Representative TEVC traces of wild-type and mutant rP2X$_7$ highlighting the differences in the rates of receptor deactivation, represented by τ, following activation by ATP or BzATP. **A**, **C**, **E** Representative TEVC traces of wild-type and mutant (R125A and R125A/I214A) rP2X$_7$ highlighting a fast rate of receptor deactivation following activation by ATP and a slow rate of receptor deactivation following activation by BzATP. **B**, **D**, **F** Representative TEVC traces of mutant (Q143A, R125A/Q143A, and R125A/Q143A/I214A) rP2X$_7$ highlighting a fast rate of receptor deactivation following activation by both ATP and BzATP. **A** TEVC traces of wild-type rP2X$_7$ highlighting the different deactivation kinetics following activation by ATP compared to BzATP. **B** TEVC traces highlighting the impact of the only single mutation (Q143A) to affect the rate of receptor deactivation. **C** TEVC traces highlighting that mutation of the residue (R125) with the biggest structural change upon BzATP binding has little effect on the rate of receptor deactivation. **D** TEVC traces highlighting that double mutations which include Q143A display a fast rate of receptor deactivation following activation by BzATP. **E** TEVC traces highlighting that the double mutation (R125A/I214A), which does not include Q143A, retains a slow rate of receptor deactivation following activation by BzATP. **F** TEVC traces highlighting that the triple mutant receptor (R125A/Q143A/I214A) has the same fast rate of receptor deactivation following activation by ATP and BzATP. The complete list of deactivation times (τ) for all wild-type and mutant constructs are included in Table 1, with data points and error bars representing the mean and standard deviation of normalized currents across triplicate experiments, respectively.

and synergistic functional effects of the three residues. The single R125A mutation, which removes the sidechain that appears, from the structure, to contribute most significantly to selective BzATP binding only moderately decreases the apparent affinity (as measured by EC_{50}) of BzATP compared to wild-type receptor without significantly affecting the apparent affinity of ATP (Fig. 4A, Table 1, Supplementary Fig. 8). The single Q143A mutation reduces the apparent affinity for both ATP and BzATP (Fig. 4A, Supplementary Fig. 8). The final single I214A mutation does not significantly affect the apparent affinity for either ATP or BzATP (Fig. 4A, Table 1, Supplementary Fig. 8). However, the effects of individual mutations are synergistic since the apparent affinity for ATP and BzATP of the double mutants (R125A/Q143A, R125A/I214A, and Q143A/I214A) and the triple mutant (R125A/Q143A/I214A) significantly decrease relative to any variant with a single mutation (Fig. 4A–C, Table 1, Supplementary Fig. 8). Importantly, mutating all three of the key residues outside the canonical orthosteric ligand-binding site of rP2X$_7$, that we identify as responsible for the coordination of BzATP, equalizes the apparent affinities of rP2X$_7$ to BzATP and ATP (Fig. 4C, Table 1). This indicates that the key to discriminating between ATP and BzATP binding resides in the identity of these three residues. Two other single mutations were performed in rP2X$_7$ to mimic residues in analogous positions from other P2X$_7$ orthologs known to affect the apparent affinity of ATP or BzATP[53,55]. A single K127A mutation was introduced into rP2X$_7$ to mimic the residue present in mouse P2X$_7$. Making this mutation in rP2X$_7$ did not appear to significantly impact the apparent affinity of either ATP or BzATP (Table 1). This is likely due to the lack of interactions between the loop containing K127 (as well as R125) in the ATP-bound open state and the importance of the R125 interactions found in the BzATP-bound open state. Next, a single I214G mutation was introduced into rP2X$_7$ to

https://doi.org/10.1038/s41467-024-50771-6

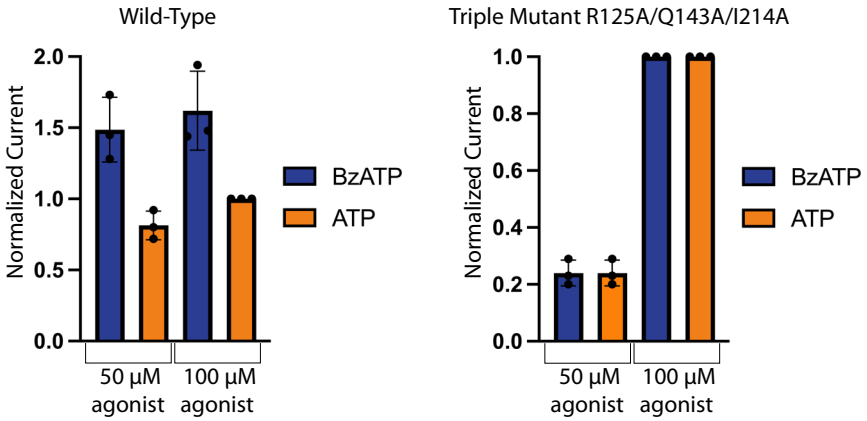

Fig. 6 | Efficacy of rP2X$_7$ activation by ATP and BzATP. (Left) Normalized current from TEVC experiments of wild-type rP2X$_7$ in response to two concentrations of ATP and BzATP, highlighting the increased normalized responses from BzATP as compared to ATP. This is consistent with BzATP acting as a full agonist and ATP as a partial agonist. (Right) Normalized current from TEVC experiments of triple mutant (R125A/Q143A/I214A) in response to two concentrations of ATP and BzATP, highlighting the virtually identical normalized responses to ATP and BzATP. The triple mutation renders BzATP and ATP equivalent agonists in terms of efficacy. Each replicate was normalized to the current from a 100 μM application of ATP so multiple oocytes could be tested. Data points and error bars represent the mean and standard deviation of normalized current across triplicate experiments, respectively.

mimic the residue present in mouse P2X$_7$. This mutation drastically reduces the apparent affinity for ATP and BzATP, consistent with prior studies on mouse P2X$_7$ (Table 1, Supplementary Fig. 8)[53]. This is likely due to the increased backbone flexibility produced by glycine which destabilizes the important loop in the dorsal fin that interacts with these agonists (Figs. 1A, 3C, E, G).

In agreement with previous work, the rate of deactivation of rP2X$_7$ is significantly slower when the receptor is activated by BzATP compared to ATP (Fig. 5A, Table 1)[53]. Intriguingly, when measuring the effect of rP2X$_7$ mutations on the apparent affinity of ATP and BzATP, it became clear that while the rate of receptor deactivation following activation by ATP does not change from any mutation, the rate of receptor deactivation following activation by BzATP increases with several different mutations (Fig. 5B–F, Table 1). To quantitate the receptor's deactivation lifetime (τ), deactivation curves from TEVC traces were fit to single or double phase decay functions and the rates of deactivation when wild-type or mutant rP2X$_7$ is activated by ATP or BzATP were determined (Table 1). Again, to our surprise, the single R125A mutation alone does not significantly change the rate of receptor deactivation following activation by BzATP, while the single Q143A mutation notably increases the rate of deactivation following activation by BzATP (Fig. 5B, C, Table 1). The single I214A mutation does not affect the rate of deactivation following activation by BzATP, while the single I214G mutation significantly increases the rate of deactivation following activation by BzATP to values similar to P2X$_7$ orthologs with a glycine residue at this position (Table 1, Supplementary Fig. 9)[53]. None of the single mutant receptors activated by BzATP demonstrated deactivation rates that were as fast as deactivation rates for wild-type receptor activated by ATP (Table 1). However, the effect of some double mutations (R125A/Q143A and Q143A/I214A) are synergistic, increasing the rate of deactivation after activation by BzATP to the wild-type rate of deactivation after activation by ATP (Fig. 5D, Table 1). Importantly, one double mutation (R125A/I214A) retains a slow rate of deactivation following activation by BzATP (Fig. 5E, Table 1). The triple mutation (R125A/Q143A/I214A) also increases the rate of receptor deactivation after activation by BzATP to that of wild-type rP2X$_7$ activated by ATP (Fig. 5F, Table 1).

Table 1 | Quantification of apparent affinity (EC_{50}) and deactivation kinetics (τ) for wild-type and mutant rP2X$_7$ activated by ATP or BzATP as measured by TEVC

Mutants	ATP EC_{50} (μM)	BzATP EC_{50} (μM)	ATP τ (s)	BzATP τ (s)
WT	34 ± 9	1.2 ± 0.2	2.0 ± 0.4*	18 ± 1.6*
R125A	41 ± 14	5 ± 1	3.5 ± 0.6	18 ± 3.7
Q143A	113 ± 30	8.5 ± 3.2	1.2 ± 0.1	7.1 ± 0.6
I214A	68 ± 11	2.5 ± 0.8	2.3 ± 1.0	21 ± 3.5*
I214G	171 ± 14	8 ± 1	2.9 ± 0.2	8.9 ± 2.2
K127A	22 ± 3	2.9 ± 0.4	2.3 ± 0.7	21 ± 6.2
R125A/Q143A	114 ± 30	18 ± 4	1.8 ± 0.1	2.5 ± 1.1
R125A/I214A	77 ± 10	14 ± 2	3.7 ± 0.8	23 ± 13
Q143A/I214A	290 ± 20	49 ± 4	2.9 ± 1.0	4.3 ± 1.7
R125A/ Q143A/I214A	203 ± 12	198 ± 60	2.4 ± 0.8	3.7 ± 0.7

The apparent affinity (EC_{50}) values and deactivation kinetics (τ) calculations represent the mean and standard deviation across triplicate experiments. For the deactivation rates, a two-component fit was required for three conditions denoted by a *: wild-type rP2X$_7$ activated by BzATP, wild-type rP2X$_7$ activated by ATP, and rP2X$_7$-I214A activated by BzATP. The two component fits are reported in the table as the amplitude weighted lifetime $\langle\tau\rangle = f_1\tau_1 + f_2\tau_2$, where f is the fractional contribution (f_i) of each decay time to the overall decay. For wild-type rP2X$_7$ activated by BzATP, this condition results in a $\tau_1 = 1.1 \pm 0.4$ s ($f_1 = 34\% \pm 1.5\%$) and $\tau_2 = 27 \pm 2.3$ s ($f_2 = 66\% \pm 1.5\%$) with an amplitude weighted lifetime $\tau = 18 \pm 1.6$ s. For wild-type rP2X$_7$ activated by ATP, this condition results in a $\tau_1 = 1.0 \pm 0.1$ s ($f_1 = 72\% \pm 4.5\%$) and $\tau_2 = 4.4 \pm 1.1$ s ($f_2 = 28\% \pm 4.5\%$) with an amplitude weighted lifetime $\tau = 2.0 \pm 0.4$ s. For wild-type rP2X$_7$-I214A activated by BzATP, this condition results in a $\tau_1 = 4.7 \pm 1.6$ s ($f_1 = 66\% \pm 2.1\%$) and $\tau_2 = 53 \pm 9.7$ s ($f_2 = 34\% \pm 2.1\%$) with an amplitude weighted lifetime $\tau = 21 \pm 3.5$ s. Two component fits have been previously observed for deactivation of P2X$_7$ by BzATP and reflect that ligand dissociation from the pocket and channel resetting to a closed pore state is likely a multi-step process[52]. The fact that the deactivation rates become mono-exponential when certain residues are mutated implicates the involvement of these residues in this multi-step process.

Previous literature has described ATP as a partial agonist and BzATP as a full agonist at P2X$_7$[31,56]. To dissect the molecular mechanisms governing partial vs. full agonism, we used TEVC to compare the absolute intensity of the currents for oocytes expressing wild-type or mutant rP2X$_7$ following activation by BzATP or ATP. As expected, for any given oocyte, wild-type rP2X$_7$ activated by BzATP results in a greater inward current than ATP at identical concentrations, consistent with properties of a full agonist compared to a partial agonist (Fig. 6). However, for oocytes expressing rP2X$_7$ containing the triple mutation (R125A/Q143A/I214A), activation by identical concentrations of ATP and BzATP result in equal current amplitudes (Fig. 6). Thus, the triple mutation (R125A/Q143A/I214A) results in a P2X$_7$ receptor with equal apparent affinity (Fig. 4C), equal rates of receptor deactivation (Fig. 5F), and equal efficacy (Fig. 6) with respect to activation by ATP and BzATP, rendering them functionally equivalent agonists. Altogether, this allows

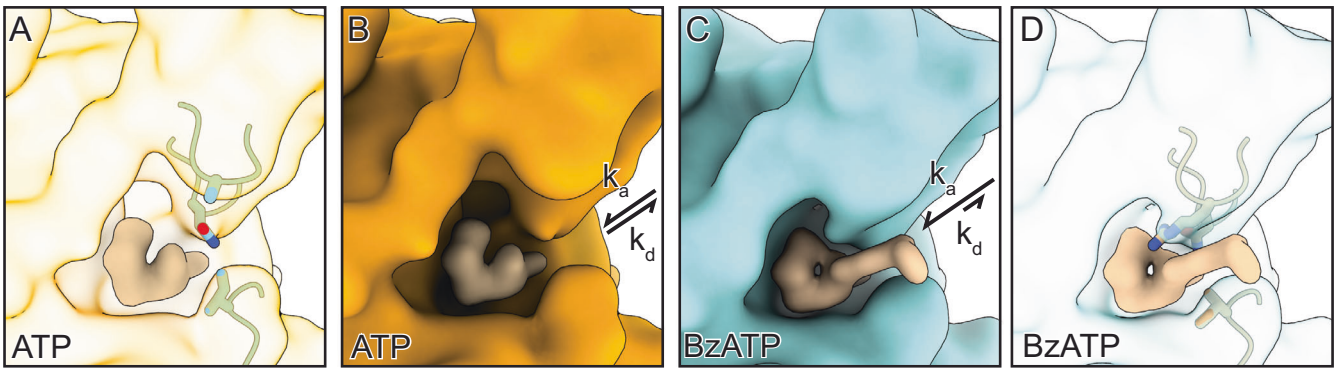

Fig. 7 | Structural basis for high-affinity agonism at the P2X$_7$ receptor. Schematic representation of the more compacted orthosteric pocket when BzATP is bound to rP2X$_7$ compared to when ATP is bound. **A** View of ATP bound in the orthosteric rP2X$_7$ ligand-binding site highlighting the positions of residues R125, Q143, and I214. Residue R125 is stubbed at the Cβ due to a lack of density in the map. **B** View of ATP bound in the orthosteric rP2X$_7$ ligand-binding site highlighting a more open pocket. **C** View of BzATP bound in the orthosteric rP2X$_7$ ligand-binding site highlighting a more compact pocket. **D** View of BzATP bound in the orthosteric rP2X$_7$ ligand-binding site highlighting the positions of residues R125, Q143, and I214. **B**, **C** Because of its key interactions with residues R125, Q143, and I214 in rP2X$_7$, BzATP has a faster association rate (k_a) and a slower dissociation rate (k_d), contributing to its higher binding affinity (equilibrium dissociation constant, K_D) compared to ATP.

us to conclude that residues R125, Q143, and I214, located just outside the canonical orthosteric ligand-binding site, are responsible for mediating each of the properties that make BzATP distinct from ATP.

Discussion

The structural and functional data associated with full-length wild-type rP2X$_7$ in apo and high-affinity agonist-bound states provide significant insights into its molecular pharmacology and unique transmembrane architecture. (1) Updated apo closed state structures of rP2X$_7$ allow placement of water molecules throughout the receptor and identification of a Na^+ ion located directly above the closed gate, revealing how the channel's pore selects a partially dehydrated Na^+ ion. (2) The significantly improved resolution of the updated apo closed state rP2X$_7$ structures visualize how three different sets of symmetry-related water molecules within the membrane interact with the backbone of the pore-lining helix (TM2) to alter its helical topology, inducing the start of, and facilitating the termination of, a short 3_{10}-helix that is responsible for correctly positioning the residues that define the receptor's closed gate. (3) BLI experiments directly measure the binding affinity (K_D) of rP2X$_7$ for ATP and BzATP, confirming that P2X$_7$ does have a lower binding affinity for ATP compared to other P2XR subtypes. (4) Structural and electrophysiological data provide an explanation for the high-affinity agonism of rP2X$_7$ by BzATP.

Visualizing ions in the pore of ion channels provides key insights into the selectivity, hydration states, and flow of ions[47,57]. The conductance pathway of P2X$_7$ begins with a preliminary constriction site formed by S339 from each protomer (Fig. 1B, C, Supplementary Fig. 5A, G). Next, a central cavity coordinates a partially hydrated Na^+ ion that is coordinated by three symmetry-related water molecules and the sidechain hydroxyl of residue S342 from each protomer (Fig. 1B). The conductance pathway of the closed state is completed by S342 from each protomer to form the closed gate of P2X$_7$ (Fig. 1B, C, Supplementary Fig. 5A, G)[35]. Interestingly, just 3 Å intracellular to the closed gate and within the pore, three additional symmetry-related water molecules are observed to interact with the sidechain hydroxyl of S342 (one water molecule interacts with the S342 hydroxyl from the corresponding protomer). Based on their location, it appears that these ordered water molecules are ideally poised to fully re-hydrate Na^+ ions once the ion channel is activated and sodium flows inward (Fig. 1B, C). We speculate the network of C3 symmetric interactions surrounding the closed gate is perfectly arranged to facilitate the octahedral coordination of Na^+, the most abundant ion in the extracellular environment. However, as the channel opens, the closed conductance pathway, formed by S342 from each protomer, dissolves to dramatically change the TM helices and create an open pore capable of non-selectively passing cations. We believe that other cations, such as Ca^{2+}, are likely never coordinated in the pore of the apo closed state. Altogether, this work reveals a structural snapshot of the conductance pathway of a Na^+ ion for P2X$_7$, laying the foundations for future work to understand ion flow through the receptor.

The updated topology of the rP2X$_7$ pore in the apo closed state, enabled by higher resolution structures, reveals a complex network of intramembrane water/protein interactions that stabilize a unique structural arrangement in TM2 to correctly set the closed gate and prevent ion flow. In the original structure of rP2X$_7$ in the apo closed state, a similar structural arrangement of TM2 was noticed, however, limited resolution prevented a molecular explanation for its unusual configuration[35]. Closely flanked by glycine residues (G338 and G345), a short 3_{10}-helix in TM2 (residues 340–344) is induced and subsequently reset with flanking helical kinks stabilized by three different sets of symmetry-related ordered water molecules located above and below the receptor gate (Fig. 1D, Supplementary Fig 4). Water molecules that induce structural changes in TM helices have been shown to play a functional role in other receptors[58,59]. However, the water mediated kinks formed from intramembrane water/protein interactions seen in P2X$_7$ have not been observed in the published apo state structures for any other P2XR subtype[35,44,50]. For P2X$_7$, formation of this 3_{10}-helix appears to play a crucial role in correctly positioning S342 from each protomer to form the gate in the apo closed conformation, which is potentially stabilized by the presence of a Na^+ ion (Fig. 1B–D). The location of S342 at the constriction gate is equivalent to that of residues in other P2XRs that have been demonstrated to impact ion selectivity, likely maintaining a role as a piece of the selectivity filter within rP2X$_7$ that regulates the passage of partially dehydrated cations (Supplementary Fig. 5, 9)[30,50,60,61]. Further, in the agonist-bound structures of rP2X$_7$, the constriction formed by S342 from each protomer defines the narrowest region of the open pore, indicating this residue remains important to the conductance pathway of the open channel (Supplementary Fig. 5).

Across P2XRs, BzATP is universally considered a more potent agonist than ATP, yet a molecular explanation for its high-affinity agonism has been unclear to this point[13,53]. In contrast to equilibrium-based radioligand assays conducted for other P2XRs, our BLI experiments provide valuable information regarding the kinetics of ligand-binding across a range of affinities. The BLI data confirm that P2X$_7$ requires more ATP in the extracellular environment than other

subtypes to bind the receptor. The higher affinity of BzATP when compared to ATP is due to a faster association to and a slower dissociation from rP2X$_7$, resulting in a correspondingly ~70-fold higher binding affinity (K_D) (Figs. 2C, D, 7). Interestingly, the rate of dissociation of BzATP from rP2X$_7$ in the BLI experiments is slower than the rate of receptor deactivation following activation by BzATP in the TEVC experiments. This may reflect differences that arise from performing kinetic BLI measurements in detergent compared to the more native membrane environment of the TEVC experiments.

The high-affinity of BzATP for P2X$_7$ is a result of three residues R125, Q143, and I214, located just outside the canonical orthosteric ligand-binding site that, upon BzATP binding, structurally rearrange to coordinate the carboxybenzophenone moiety of BzATP (Fig. 7A, D). Across rat, mouse, and human P2X$_7$, R125 and Q143 are conserved while there is an I214G substitution in the mouse ortholog (Supplementary Fig. 9). Interestingly, sequence alignments indicate that these residues are not conserved across other P2XR subtypes (Supplementary Fig. 9). Structurally, R125, Q143, and I214 are similarly positioned to K113, P128, and M200 in hP2X$_3$ (PDB code: 5SVK) and T124, R143, and L217 in zfP2X$_4$ (PDB code: 4DW1), showing that BzATP is coordinated by a unique set of residues for each P2XR that likely play a role in its subtype-selectivity[50,51].

The roles of R125, Q143, and I214 in high-affinity BzATP binding can be interpreted from the electrophysiology data. Since the ratio of k_d to k_a is the equilibrium dissociation constant, K_D, evaluating how selective residue mutations affect apparent affinity (EC_{50}) and rate of receptor deactivation (τ) can provide insight into how the mutations impact BzATP and ATP binding relative to the wild-type receptor. For example, we can conclude that residue R125 plays a role in facilitating the association of BzATP to rP2X$_7$. This is because an alanine mutation at this residue position reduces the receptor's apparent affinity for BzATP without altering the rate of receptor deactivation (Figs. 4A, 5C, Table 1, Supplementary Fig. 8). This can only happen if the alanine mutation impacts (by decreasing) the rate of ligand association. On the other hand, residue Q143 seems to be responsible for slowing the dissociation of BzATP from rP2X$_7$ because when mutated to alanine, the rate of receptor deactivation increases and correlatively, the apparent affinity for BzATP decreases (Figs. 4A, 5B, Table 1, Supplementary Fig. 8). Finally, mutation of I214 on its own has little impact on the apparent affinity of ATP or BzATP to rP2X$_7$, however in conjunction with other mutations, mutating this residue appears to have synergistic effects. Any single mutation to the three residues structurally responsible for BzATP-binding does not nullify the high-affinity binding of BzATP relative to ATP for rP2X$_7$, so multiple residues must play a synergetic role to facilitate high-affinity agonism by BzATP. Examining the results from two mutant receptors highlights the impact of residues on high-affinity BzATP agonism. The double mutation R125A/I214A decreases apparent affinity without altering rates of receptor deactivation, confirming Q143 is key for slowing the dissociation of BzATP from the receptor. However, only the triple mutation (R125A/Q143A/I214A) is ultimately able to effectively passivate the slower dissociation and eliminate the high-affinity agonism of BzATP to rP2X$_7$. Thus, the ability of rP2X$_7$ to discriminate between ATP and BzATP resides in how residues R125, Q143, and I214 interact with each ligand.

The structural and functional data provided here define ion coordination and the conductance pathway in the apo closed state as well as high-affinity agonism for the rP2X$_7$ receptor. A partially hydrated Na^+ ion sits directly above the closed gate with one set of waters poised in the pore just below, revealing how partially hydrated ions can contribute to the stability of the closed channel and suggests a mechanism for ion re-hydration upon pore opening. Three different sets of symmetry-related ordered water molecules, one set within the pore and above the gate and the other two sets below the gate and within the transmembrane domain, directly impact the helical topology of TM2, correctly positioning residues to stabilize the closed gate. The universal P2XR agonist, BzATP, interacts with three residues just outside of the canonical P2X$_7$ orthosteric ligand-binding site. These interactions promote ligand entry into the binding pocket and cause the receptor to clamp onto the ligand by forming a more compact pocket, slowing its release (Fig. 7). Thus, these ligand-receptor interactions both increase BzATP association to the receptor and slow BzATP dissociation from the receptor, enabling its high-affinity agonism. The faster association of BzATP to rP2X$_7$ is likely a combination of several factors: steric bulk of the carboxybenzophenone moiety limits the potential for orientation sampling of the ligand and the positively charged sidechain of R125 interacts with the carboxybenzophenone moiety to provide an initial binding step to facilitate BzATP entry into the pocket. The slower dissociation of BzATP from rP2X$_7$ is likely an effect of the increased network of interactions that stabilize the ligand when bound, predominately mediated by Q143. Leveraging these molecular insights, new iterations of P2X$_7$ agonists can be developed to optimize the interactions responsible for the high-affinity of BzATP. Altogether, our results explain the structural and functional foundations of high-affinity BzATP agonism, providing pivotal considerations for the development of P2XR agonists, which might be important experimental tools to study or effective therapeutic approaches to treat several forms of cancer[26].

Methods

Ethical statement

Unfertilized *Xenopus laevis* oocytes were purchased through Ecocyte Biosciences and kept at 18 °C until injection. This research complies with all relevant ethical regulations. All surgical procedures for isolation of Xenopus laevis oocytes were done in accordance with animal welfare laws, followed national and institutional guidelines for humane animal treatment and complied with relevant legislation. Ecocyte Biocience protocols help reduce the stress and harm on the laboratory animals, and appropriate aftercare such as pain management is employed to further minimize the impact of surgeries on the animals.

Cell Lines

SF9 cells were cultured in SF-900 III SFM (Fisher Scientific) at 27 °C. Cells of female origin were used for the expression of baculovirus. HEK293 GNTI$^-$ cells were cultured using Gibco Freestyle 293 Expression Medium (Fisher Scientific) at 37 °C supplemented with 2% v/v fetal bovine serum (FBS)[62]. HEK293 cells of female origin were used to express receptor.

Receptor constructs

The full-length wild-type rP2X$_7$ construct used for structure determination has been previously described[35]. No mutations or truncations were made to the receptor for structure determination. For electrophysiology experiments, the rP2X$_7$-WT construct is unmodified, full-length wild-type rP2X$_7$ with no GFP, protease sites, or affinity tags present. All mutagenesis was performed using QuikChange XL mutagenesis kits (Agilent Technologies) from this initial WT construct to create mutant receptors: rP2X$_7$-R125A, rP2X$_7$-R127A, rP2X$_7$-Q143A, rP2X$_7$-I214A, rP2X$_7$-I214G, rP2X$_7$-R125A/Q143A, rP2X$_7$-R125A/I214A, rP2X$_7$-Q143A/I214A, and rP2X$_7$-R125A/Q143A/I214A.

Receptor expression and purification

The full-length wild-type rP2X$_7$ construct was expressed by baculovirus mediated gene transfection (BacMam) using identical protocols as previously outlined[35]. Briefly, HEK293 GNTI$^-$ cells were grown in suspension to a sufficient density and infected with P2 BacMam virus. Following overnight growth at 37 °C, sodium butyrate was added (final concentration of 10 mM) and cells shifted to 30 °C for an additional 48 hours. After such time, the cells were harvested, washed with PBS buffer (137 mM NaCl, 2.7 mM KCl, 8 mM Na_2HPO_4, 2 mM KH_2PO_4),

suspended in TBS (50 mM Tris pH 8.0, 150 mM NaCl) containing protease inhibitors (1 mM PMSF, 0.05 mg/mL aprotinin, 2 mg/mL Pepstatin A, 2 mg/mL leupeptin), and broken via sonication. Intact cells and cellular debris were removed by centrifugation and then membranes isolated by ultracentrifugation. The membranes were snap frozen and stored at −80 °C until use.

Membranes were thawed, resuspended in TBS buffer containing 15% glycerol, dounce homogenized, and then solubilized in 40 mM dodecyl-β-D-maltopyranoside (DDM or C12M) and 8 mM cholesterol hemisuccinate tris salt (CHS). The soluble fraction was isolated by ultracentrifugation and incubated with TALON resin in the presence of 10 mM imidazole at 4 °C for 1–2 h. After packing into an XK-16 column, the purification column was washed with 2 column volumes of buffer (TBS plus 5% glycerol, 1 mM C12M, 0.2 mM CHS at pH 8.0) containing 20 mM imidazole, 10 column volumes containing 30 mM imidazole, and eluted with buffer containing 250 mM imidazole. Peak fractions containing the protein were concentrated and digested with HRV 3-C protease (1:25, w/w) at 4 °C overnight. The digested protein was then ultracentrifuged and injected onto a Superdex 200 10/300 GL column for size exclusion chromatography (SEC) using buffer equilibrated with 20 mM HEPES, pH 7.0, 100 mM NaCl, and 0.5 mM C12M. Fractions were analyzed by SDS-PAGE and fluorescence size exclusion chromatography (FSEC), pooled accordingly, and concentrated for cryo-EM grid preparation. For the sample in the absence of sodium, sodium buffers were replaced with potassium buffers across all purification steps.

Electron microscopy sample preparation

To prepare the BzATP-rP2X$_7$ sample, the purified receptor was incubated with BzATP at 400 μM (Alomone Labs). After a one-hour incubation and ultracentrifugation, cryo-EM grids were prepared for each rP2X$_7$ sample. Specifically, for all apo samples 2.5 μL of sample was applied to glow-discharged (15 mA, 1 min) Quantifoil R1.2/1.3 300 mesh gold holey carbon grids which were blotted for 1.5 s under 100% humidity at 6 °C. For the BzATP-containing condition, sample was applied twice, blotting in-between to achieve adequate particle concentrations. The grids were then flash frozen in liquid ethane using a FEI Vitrobot Mark IV and stored under liquid nitrogen until screening and large-scale data acquisition.

Electron microscopy data acquisition

Cryo-EM datasets for all receptor complexes were collected on Titan Krios microscopes (FEI) operated at 300 kV at the Pacific Northwest Center for Cryo-EM (PNCC). Datasets were acquired on microscopes with an energy filter (Gatan Image Filter, 20 eV slit width) and a Gatan K3 direct-electron detector. All movies were collected in super-resolution mode at a nominal magnification of ×130,000, corresponding to a physical pixel size of ~0.648 Å/pixel, using a defocus range of −0.8 to −1.5 μm and total dose of between 40 and 45 e$^-$/ Å^2. Each dataset utilized 'multi-shot' and 'multi-hole' collection schemes driven by serialEM to maximize high-throughput data collection[63].

Electron microscopy data processing

Super-resolution image stacks were motion corrected and binned in cryoSPARC V3 using patch motion correction (Supplementary Fig. 2, Supplementary Table 1)[64]. The contrast transfer function (CTF) parameters were estimated in cryoSPARC using patch CTF estimation and particles picked using 2D templates. Micrographs and particle picks were curated and after extraction, particles were classified using iterative ab initio and heterogenous classifications (Supplementary Fig. 2). No 2D classification was performed for any dataset. The final homogenous particle stack was re-extracted at the physical pixel size (0.648 Å/pixel), CTF correction at the global and local scales performed, and a final non-uniform refinement generated the consensus cryo-EM map (Supplementary Fig. 2, 3, Supplementary Table 1).

Model building and structure determination

The models were built in Coot v0.9.8 based upon initial models of rP2X$_7$ in either the apo closed state (PDB code: 6U9V) or ATP-bound open state (PDB code: 6U9W)[35,65]. The closed state structure 6U9V was used for apo models, while the open state structure 6U9W was used for the initial model of the high-affinity agonist BzATP bound to rP2X$_7$. BzATP and its corresponding CIF file were built in eLBOW with protonation states corresponding to approximately pH 7[66]. All stages of model building involved manual adjustments based on the quality of the maps in Coot, followed by real space refinement in PHENIX v1.18[67]. Limited glycosylation and acylation were included in the models when justified by density. In some of the models, sidechains for residues were not included if sufficient density was not apparent. Some heteroatoms were renumbered from the initial models to facilitate comparison between the final models. Model quality was evaluated by MolProbity (Supplementary Table 1)[68].

In silico ΔΔG calculations

The ΔΔG calculations were performed within Rosetta using the all-atom scoring function[54]. Briefly, single-point or sets of mutations for the BzATP-bound rP2X$_7$ structure were made in Coot and the scoring function performed using parameter files for ligands or unknown residues. Mutant receptor ΔG scores were then subtracted from the wild-type ΔG score to determine the ΔΔG score for the mutant construct.

Two-electrode voltage clamping

Preparation of oocytes expressing rP2X$_7$. *Xenopus Laevis* oocytes were purchased defolliculated from Ecocyte Biosciences and resuspended in Modified Barth's Solution 88 mM NaCl, 1 mM KCl, 0.82 mM $MgSO_4$, 0.33 mM $Ca(NO_3)_2{\cdot}4H_2O$, 0.41 mM $CaCl_2{\cdot}2H_2O$, 2.4 mM $NaHCO_3$, 5 mM HEPES supplemented with amikacin 250 mg/L and gentamycin 150 mg/L. Oocytes were then injected with 50 nL of 10 ng/μL rP2X$_7$ mRNA that was made from linearized full-length wild-type or mutant pcDNA 3.1x according to the protocol provided in the mMessage mMachine kit (Invitrogen). Injected ooctyes were allowed to express for ~20 hours before recording was performed.

TEVC recordings. Data acquisition was performed using the Ooctye Clamp OC-725C amplifier and pClamp 8.2 software. Buffers were applied using a gravity fed RSC-200 Rapid Solution Changer that flows at ~5 mL/min. All experiments use Sutter filamented glass 10 cm in length with an inner diameter of 0.69 mm and an outer diameter of 1.2 mm to impale oocytes and clamp the holding voltage at −60 mV. Experiments were recorded in buffer containing 100 mM NaCl, 2.5 mM KCl, 0.1 mM EDTA, 0.1 mM flufenamic acid, and 5 mM HEPES at pH 7.4. All oocytes expressing wild-type and mutant P2X$_7$ were facilitated with 100 μM before any final data was recorded.

Dose response (EC$_{50}$) experiments. Excitatory responses to a dilution series of ATP consisting of 1.5 mM, 500 μM, 166 μM, 55 μM, 19 μM, 6 μM, and 2 μM were examined. Dilution series experiments using BzATP were performed at concentrations of 300 μM, 100 μM, 33 μM, 11 μM, 3.7 μM, 1.2 μM, 0.41 μM, and 0.14 μM. Each evoked response was normalized to the signal evoked by the largest concentration and the data was fitted in Prism 9 using the nonlinear regression named "EC$_{50}$, x is concentration" to afford EC$_{50}$ values. This value is then averaged amongst each singular condition and reported as an average plus or minus the standard deviation.

Assessing deactivation time (τ) experiments. Currents were evoked by application of 100 μM ATP or 10 μM BzATP and deactivation was observed. The triple mutant (Q143A/R125A/I214A) required 100 μM BzATP to generate traces for deactivation time experiments. Each condition was completed in triplicate for the first, second, and third application of a single ligand to a single oocyte condition. Average

deactivation times (τ) were calculated using either Prism 9 or RStudio software to fit each TEVC tracing to a one- or two-phase decay function, respectively, and obtain a value τ. To determine the correct model for each mutation and agonist, data was fit to one- and two-phase decay functions to generate R^2 values. The simplest model was chosen that allowed for an adjusted R^2 value of 0.99 or greater. In cases where the two-phase model did not reach a plateau, the one-phase decay model was chosen by default. The τ values of each singular condition were averaged and reported as an average plus or minus the standard deviation.

Efficacy experiments. An initial excitatory response to 100 μM ATP was recorded from each oocyte for normalization. This was followed by a 50 μM ATP application, and then a 50 μM BzATP application for oocytes expressing either the wild-type or triple mutant (Q143A/R125A/I214A) receptor. The concentration was then increased to 100 μM ATP and 100 μM BzATP, and evoked currents were again recorded for oocytes expressing either the wild-type or triple mutant (Q143A/R125A/I214A) receptor. After each application of agonist, currents were returned to baseline with application of recording buffer. Each concentration was tested in triplicate per receptor construct and graphed on a scatter bar graph using Prism 9.

In vitro biotinylation of $rP2X_7$

Purified $rP2X_7$ was diluted to 1 mL and desalted into PBS buffer (pH 7.4) using a HiTrap desalting column (Cytiva). Desalted fractions containing $rP2X_7$ were pooled and concentrated before adjusting the pH to 8.0 with $NaHCO_3$. NHS-ester-PEG12-biotin (ThermoFisher) was added and incubated at 23 °C for 60 min with shaking. The biotinylated sample was then diluted with PBS and concentrated. Dilution and concentration was repeated four more times to remove free NHS-ester-PEG12-biotin in a 100 kDa concentrator (Millipore Sigma). After final concentration, the absorbance at 280 nm was taken to quantify the concentration of biotinylated $rP2X_7$.

BLI for affinity determination

BLI experiments were carried out on a ForteBio Octet RED384 instrument with ForteBio Data Acquisition software 11.0. The assays were performed at 30 °C in 384-well tilted-bottom plates (Sartorius) with orbital shaking at 1,000 r.p.m. Running buffer consisted of filtered (0.22 μm) PBS (pH 7.4) and 0.5 mM DDM (Anatrace). SA biosensor tips (Sartorius) were pre-equilibrated in running buffer for 20 min and loaded with 50 μg ml^{-1} of biotinylated $rP2X_7$ ligand or biocytin (Sigma-Aldrich) control for 1800 s. Next, the loaded SA sensors were blocked with 100 μg ml^{-1} of biocytin for 150 s and then washed with running buffer for 60 s. All loaded sensors were then baselined in running buffer for 120 s and dipped into wells containing threefold dilutions (30 to 0.12 μM for ATP or 3.3 to 0.014 μM for BzATP) for 90 s and then returned to running buffer for the dissociation step for 300 s for ATP or 800 s for BzATP. After data collection, rate constants for association and dissociation were determined using ForteBio Data Analysis HT 11.0 evaluation software. To maximize signal between the large ligand and small analyte, the raw data were double reference subtracted. The first subtraction was biocytin controls across analyte concentrations and the second, at the zero-analyte concentration. Using biocytin for a parallel reference has been described previously and is an adequate and generalizable method to quantify nonspecific binding to sensors at different analyte concentrations, independent of the protein system being studied[69]. Biocytin binds to the streptavidin (SA) biosensors to eliminate non-specific binding of the analyte to the sensor. For each interaction pair, the association rate constant (k_a) and the dissociation rate constant (k_d) were calculated with an average of three independent assays with at least four different concentrations that were globally fit to a 1:1 Langmuir binding model. The equilibrium dissociation constant (K_D) was calculated as the ratio of k_d to k_a. The K_D, k_a, and k_d values are reported as the average ± the standard deviation of three replicate datasets for each analyte, with each dataset using at least four independent traces. The analyzed data were exported and plotted in GraphPad Prism 9.0.

Reporting summary

Further information on research design is available in the Nature Portfolio Reporting Summary linked to this article.

Data availability

All cryo-EM density maps for the full-length wild-type $rP2X_7$ receptor in the apo and agonist-bound states have been deposited in the EM Database under the EMDB accession codes: EMD-41570 (apo NaCl), EMD-42976 (apo KCl), and EMD-41581 (BzATP). The maps within these depositions include both half maps, sharpened/unsharpened maps, refinement masks, and any local refinements or locally sharpened maps that helped with model building. The corresponding coordinates for the structures have been deposited in Protein Data Bank under the PDB accession codes: 8TR5 (apo NaCl), 8V4S (apo KCl), and 8TRJ (BzATP). The ATP-bound open state structure of $rP2X_7$ was obtained using the PDB code 6U9W. The source data underlying Figs. 2B–D, 4A–C, 5A-F, 6, Table 1, and Supplementary Fig. 8 are provided as a Source Data file. Source data are provided with this paper.

References

1. Hinkle, P. C. & McCarty, R. E. How cells make ATP. *Sci. Am.* **238**, 104–123 (1978).
2. Roman, R. M. & Fitz, J. G. Emerging roles of purinergic signaling in gastrointestinal epithelial secretion and hepatobiliary function. *Gastroenterology* **116**, 964–979 (1999).
3. Taylor, A. L. et al. Epithelial P2X purinergic receptor channel expression and function. *J. Clin. Invest* **104**, 875–884 (1999).
4. Burnstock, G. Purinergic nerves. *Pharm. Rev.* **24**, 509–581 (1972).
5. Burnstock, G. Introduction: P2 receptors. *Curr. Top. Med Chem.* **4**, 793–803 (2004).
6. Webb, T. E. et al. Cloning and functional expression of a brain G-protein-coupled ATP receptor. *FEBS Lett.* **324**, 219–225 (1993).
7. Brake, A. J., Wagenbach, M. J. & Julius, D. New structural motif for ligand-gated ion channels defined by an ionotropic ATP receptor. *Nature* **371**, 519–523 (1994).
8. North, R. A. Molecular physiology of P2X receptors. *Physiol. Rev.* **82**, 1013–1067 (2002).
9. Valera, S. et al. A new class of ligand-gated ion channel defined by P2x receptor for extracellular ATP. *Nature* **371**, 516–519 (1994).
10. Murrell-Lagnado, R. D. & Qureshi, O. S. Assembly and trafficking of P2X purinergic receptors (Review). *Mol. Membr. Biol.* **25**, 321–331 (2008).
11. Saul, A., Hausmann, R., Kless, A. & Nicke, A. Heteromeric assembly of P2X subunits. *Front Cell Neurosci.* **7**, 250 (2013).
12. Burnstock, G. & Kennedy, C. P2X receptors in health and disease. *Adv. Pharm.* **61**, 333–372 (2011).
13. Illes, P. et al. Update of P2X receptor properties and their pharmacology: IUPHAR Review 30. *Br. J. Pharm.* **178**, 489–514 (2021).
14. Baljit, S. K. et al. International Union of Pharmacology. XXIV. Current Status of the Nomenclature and Properties of P2X Receptors and Their Subunits. *Pharmacol. Rev.* **53**, 107 (2001).
15. Jarvis, M. F. & Khakh, B. S. ATP-gated P2X cation-channels. *Neuropharmacology* **56**, 208–215 (2009).
16. Werner, P., Seward, E. P., Buell, G. N. & North, R. A. Domains of P2X receptors involved in desensitization. *Proc. Natl Acad. Sci. USA* **93**, 15485–15490 (1996).
17. Kawate, T. P2X Receptor Activation. *Adv. Exp. Med Biol.* **1051**, 55–69 (2017).
18. Mansoor, S. E. How structural biology has directly impacted our understanding of P2X receptor function and gating. in *The P2X7 Receptor*. (ed. Nicke, A.) (Humana New York, NY, in press) (2022).

19. Bianchi, B. R. et al. Pharmacological characterization of recombinant human and rat P2X receptor subtypes. *Eur. J. Pharmacol.* **376**, 127–138 (1999).
20. Kamei, J., Takahashi, Y., Yoshikawa, Y. & Saitoh, A. Involvement of P2X receptor subtypes in ATP-induced enhancement of the cough reflex sensitivity. *Eur. J. Pharm.* **528**, 158–161 (2005).
21. Mahaut-Smith, M. P., Jones, S. & Evans, R. J. The P2X1 receptor and platelet function. *Purinergic Signal* **7**, 341–356 (2011).
22. Yan, D. et al. Mutation of the ATP-gated P2X2 receptor leads to progressive hearing loss and increased susceptibility to noise. *Proc. Natl Acad. Sci.* **110**, 2228–2233 (2013).
23. Burnstock, G. & Knight, G. E. The potential of P2X7 receptors as a therapeutic target, including inflammation and tumour progression. *Purinergic Signal* **14**, 1–18 (2018).
24. Lara, R. et al. P2X7 in cancer: From molecular mechanisms to therapeutics. *Front Pharm.* **11**, 793 (2020).
25. North, R. A. & Jarvis, M. F. P2X receptors as drug targets. *Mol. Pharm.* **83**, 759–769 (2013).
26. Roger, S. et al. Understanding the roles of the P2X7 receptor in solid tumour progression and therapeutic perspectives. *Biochimica et. Biophysica Acta (BBA)—Biomembranes* **1848**, 2584–2602 (2015).
27. Keystone, E. C. et al. Clinical evaluation of the efficacy of the P2X7 purinergic receptor antagonist AZD9056 on the signs and symptoms of rheumatoid arthritis in patients with active disease despite treatment with methotrexate or sulphasalazine. *Ann. Rheum. Dis.* **71**, 1630–1635 (2012).
28. Abdulqawi, R. et al. P2X3 receptor antagonist (AF-219) in refractory chronic cough: a randomised, double-blind, placebo-controlled phase 2 study. *Lancet* **385**, 1198–1205 (2015).
29. CCTU-Core, Pharmaceuticals, J., Cambridgeshire & Trust, P.N.F. Antidepressant trial with P2X7 antagonist JNJ-54175446. (https://ClinicalTrials.gov/show/NCT04116606 2019).
30. Oken, A. C. et al. Molecular pharmacology of P2X receptors: Exploring druggable domains revealed by structural biology. *Front. Pharmacol.* **13**, 925880 (2022).
31. Donnelly-Roberts, D. L., Namovic, M. T., Han, P. & Jarvis, M. F. Mammalian P2X7 receptor pharmacology: Comparison of recombinant mouse, rat and human P2X7 receptors. *Br. J. Pharm.* **157**, 1203–1214 (2009).
32. Clare, A. J. et al. Functional regulation of P2X6 receptors by N-linked glycosylation: Identification of a novel alpha beta-methylene ATP-sensitive phenotype. *Mol. Pharmacol.* **65**, 979 (2004).
33. Jiang, R. et al. Tightening of the ATP-binding sites induces the opening of P2X receptor channels. *EMBO J.* **31**, 2134–2143 (2012).
34. Surprenant, A., Rassendren, F., Kawashima, E., North, R. A. & Buell, G. The cytolytic P2Z receptor for extracellular ATP identified as a P2X receptor (P2X7). *Science* **272**, 735–738 (1996).
35. McCarthy, A. E., Yoshioka, C. & Mansoor, S. E. Full-Length P2X7 structures reveal how palmitoylation prevents channel desensitization. *Cell* **179**, 659–670 e13 (2019).
36. Di Virgilio, F. The P2Z purinoceptor: an intriguing role in immunity, inflammation and cell death. *Immunol. Today* **16**, 524–528 (1995).
37. Pelegrin, P. P2X7 receptor and the NLRP3 inflammasome: Partners in crime. *Biochem Pharm.* **187**, 114385 (2021).
38. Bian, S. et al. P2X7Integrates PI3K/AKT and AMPK-PRAS40-mTOR signaling pathways to mediate tumor cell death. *PLOS ONE* **8**, e60184 (2013).
39. Wang, W., Xiao, J., Adachi, M., Liu, Z. & Zhou, J. 4-aminopyridine induces apoptosis of human acute myeloid leukemia cells via increasing [Ca2+]i through P2X7 receptor pathway. *Cell. Physiol. Biochem.* **28**, 199–208 (2011).
40. Zhou, J. Z. et al. Differential impact of adenosine nucleotides released by osteocytes on breast cancer growth and bone metastasis. *Oncogene* **34**, 1831–1842 (2015).
41. Karasawa, A. & Kawate, T. Structural basis for subtype-specific inhibition of the P2X7 receptor. *Elife* **5**, e22153 (2016).
42. Kasuya, G. et al. Structural insights into the competitive inhibition of the ATP-gated P2X receptor channel. *Nat. Commun.* **8**, 876 (2017).
43. Sheng, D. et al. Structural insights into the orthosteric inhibition of P2X receptors by non-ATP-analog antagonists. (eLife Sciences Publications, Ltd, 2023).
44. Kawate, T., Michel, J. C., Birdsong, W. T. & Gouaux, E. Crystal structure of the ATP-gated P2X(4) ion channel in the closed state. *Nature* **460**, 592–598 (2009).
45. Lionta, E., Spyrou, G., Vassilatis, D. K. & Cournia, Z. Structure-based virtual screening for drug discovery: principles, applications and recent advances. *Curr. Top. Med Chem.* **14**, 1923–1938 (2014).
46. Batool, M., Ahmad, B. & Choi, S. A structure-based drug discovery paradigm. *Int J. Mol. Sci.* **20**, 2783 (2019).
47. Gouaux, E. & Mackinnon, R. Principles of selective ion transport in channels and pumps. *Science* **310**, 1461–1465 (2005).
48. Gucwa, M. et al. CMM—An enhanced platform for interactive validation of metal binding sites. *Protein Sci.* **32**, e4525 (2023).
49. Shah, N. B. & Duncan, T. M. Bio-layer interferometry for measuring kinetics of protein-protein interactions and allosteric ligand effects. *JoVE*, e51383 (2014).
50. Mansoor, S. E. et al. X-ray structures define human P2X(3) receptor gating cycle and antagonist action. *Nature* **538**, 66–71 (2016).
51. Hattori, M. & Gouaux, E. Molecular mechanism of ATP binding and ion channel activation in P2X receptors. *Nature* **485**, 207–212 (2012).
52. Yan, Z., Khadra, A., Sherman, A. & Stojilkovic, S. S. Calcium-dependent block of P2X7 receptor channel function is allosteric. *J. Gen. Physiol.* **138**, 437–452 (2011).
53. Hibell, A. et al. Species- and agonist-dependent differences in the deactivation-kinetics of P2X7 receptors. *Naunyn-Schmiedeberg's. Arch. Pharmacol.* **363**, 639–648 (2001).
54. Alford, R. F. et al. The Rosetta all-atom energy function for macromolecular modeling and design. *J. Chem. Theory Comput* **13**, 3031–3048 (2017).
55. Mark, T. Y., Pablo, P. & Annmarie, S. Amino acid residues in the P2X7 receptor that mediate differential sensitivity to ATP and BzATP. *Mol. Pharmacol.* **71**, 92 (2007).
56. Wiley, J. S., Gargett, C. E., Zhang, W., Snook, M. B. & Jamieson, G. P. Partial agonists and antagonists reveal a second permeability state of human lymphocyte P2Z/P2X7 channel. *Am. J. Physiol.-Cell Physiol.* **275**, C1224–C1231 (1998).
57. Zhou, Y., Morais-Cabral, J. H., Kaufman, A. & MacKinnon, R. Chemistry of ion coordination and hydration revealed by a K+ channel–Fab complex at 2.0 Å resolution. *Nature* **414**, 43–48 (2001).
58. Miyano, M., Ago, H., Saino, H., Hori, T. & Ida, K. Internally bridging water molecule in transmembrane α-helical kink. *Curr. Opin. Struct. Biol.* **20**, 456–463 (2010).
59. Alam, A. & Jiang, Y. High-resolution structure of the open NaK channel. *Nat. Struct. Mol. Biol.* **16**, 30–34 (2009).
60. Terrance, M. E. & Baljit, S. K. Contribution of calcium ions to P2X channel responses. *J. Neurosci.* **24**, 3413 (2004).
61. Migita, K., Haines, W. R., Voigt, M. M. & Egan, T. M. Polar residues of the second transmembrane domain influence cation permeability of the ATP-gated P2X2 receptor*. *J. Biol. Chem.* **276**, 30934–30941 (2001).
62. Reeves, P. J., Callewaert, N., Contreras, R. & Khorana, H. G. Structure and function in rhodopsin: High-level expression of rhodopsin with restricted and homogeneous N-glycosylation by a tetracycline-inducible N-acetylglucosaminyltransferase I-negative HEK293S stable mammalian cell line. *Proc. Natl Acad. Sci.* **99**, 13419–13424 (2002).
63. Mastronarde, D. N. Automated electron microscope tomography using robust prediction of specimen movements. *J. Struct. Biol.* **152**, 36–51 (2005).

64. Punjani, A., Rubinstein, J. L., Fleet, D. J. & Brubaker, M. A. cryoSPARC: algorithms for rapid unsupervised cryo-EM structure determination. *Nat. Methods* **14**, 290–296 (2017).
65. Emsley, P., Lohkamp, B., Scott, W. G. & Cowtan, K. Features and development of coot. *Acta Crystallogr. Sect. D.* **66**, 486–501 (2010).
66. Moriarty, N. W., Grosse-Kunstleve, R. W. & Adams, P. D. Electronic ligand builder and optimization workbench (eLBOW):A tool for ligand coordinate and restraint generation. *Acta Crystallogr. Sect. D.* **65**, 1074–1080 (2009).
67. Liebschner, D. et al. Macromolecular structure determination using X-rays, neutrons and electrons: recent developments in Phenix. *Acta Crystallogr. Sect. D.* **75**, 861–877 (2019).
68. Williams, C. J. et al. MolProbity: More and better reference data for improved all-atom structure validation. *Protein Sci.* **27**, 293–315 (2018).
69. Wang, L. G. et al. OregonFluor enables quantitative intracellular paired agent imaging to assess drug target availability in live cells and tissues. *Nat. Chem.* **15**, 729–739 (2023).
70. Meng, E. C. et al. UCSF ChimeraX: Tools for structure building and analysis. *Protein Sci.* **32**, e4792 (2023).

Acknowledgements

We thank T. Humphreys, O. Davulcu, C. Yoshioka, and C. López at PNCC for access and microscopy assistance; K. Tao and M. Gomez for BLI assistance; J. Savage, U. Shinde, and D. Farrens for figure and manuscript feedback. Electron microscopy grid screening was performed at the Multiscale Microscopy Core within Oregon Health & Science University (OHSU). A portion of this research was supported by NIH grant U24GM129547 and performed at the PNCC at OHSU and accessed through EMSL (grid.436923.9), a DOE Office of Science User Facility sponsored by the Office of Biological and Environmental Research. This research was supported by the National Heart, Lung and Blood Institute (R00HL138129, S.E.M.), the National Institute of General Medical Sciences (DP2GM149551, S.E.M.), and the American Heart Association (24PRE1195450, A.C.O.).

Author contributions

A.C.O. and S.E.M. designed the project. I.K., A.E.M., A.G., and A.C.O. performed sample preparation for cryo-EM and biochemistry studies. A.C.O. performed the cryo-EM data collection. A.C.O., I.K., A.G., and M.H.G. analyzed the cryo-EM data. A.O., I.K., A.G., S.E.M., and M.H.G. built the cryo-EM models. A.C.O. performed and analyzed the BLI experiments. A.C.O., N.E.L., and S.E.M. performed and analyzed the electrophysiological experiments. A.C.O., N.E.L., and S.E.M. wrote the manuscript. All authors edited the manuscript.

Competing interests

The authors declare no competing interests.

Additional information

Supplementary information The online version contains supplementary material available at https://doi.org/10.1038/s41467-024-50771-6.

Correspondence and requests for materials should be addressed to Steven E. Mansoor.

Peer review information : *Nature Communications* thanks Annette Nicke and Shujia Zhu for their contribution to the peer review of this work. A peer review file is available.